ENGINEERING

# Ultrafast rectifying counter-directional transport of proton and metal ions in metal-organic framework–based nanochannels

**Jun Lu[1]†, Hengyu Xu[2]†, Hao Yu[2]†, Xiaoyi Hu[1]†, Jun Xia[2], Yinlong Zhu[1], Fengchao Wang[2], Heng-An Wu[2]*, Lei Jiang[1], Huanting Wang[1]***



**Bioinspired control of ion transport at the subnanoscale has become a major focus in the fields of nanofluidics and membrane separation. It is fundamentally important to achieve rectifying ion-specific transport in artificial ion channels, but it remains a challenge. Here, we report a previously unidentified metal-organic framework nanochannel (MOF NC) nanofluidic system to achieve unidirectional ultrafast counter-directional transport of alkaline metal ions and proton. This highly effective ion-specific rectifying transport behavior is attributed to two distinct mechanisms for metal ions and proton, elucidated by theoretical simulations. Notably, the MOF NC exhibits ultrafast proton conduction stemming from ultrahigh proton mobility, i.e., $11.3 \times 10^{-7}$ $m^2$ /V·s, and low energy barrier of 0.075 eV in MIL-53-COOH subnanochannels. Furthermore, the MOF NC shows excellent osmotic power–harvesting performance in reverse electrodialysis. This work expects to inspire further research into multifunctional biomimetic ion channels for advanced nanofluidics, biomimetics, and separation applications.**

## INTRODUCTION

Directional ultrafast transport of ions with atomic-scale precision is one of the core functions of biological ion channels in cell membranes (*1*–*5*). For example, inwardly rectifying potassium channel can unidirectionally transport $K^+$ from the extracellular to the intracellular side of cells, while some biological proton channels can exhibit preferential proton transport in the opposite direction (Fig. 1A-i). These biological ion channels cooperatively maintain the electrolyte and pH balance across cell membranes, which are essential for the physiological activities of the cells. For example, the electrolyte concentration disorder in cells, especially for the cations such as $K^+$, $Na^+$, and proton, is recognized to have direct link with some diseases such as epilepsy (*5*, *6*). Inspired by these functions, artificial macroscopic nanochannel (NC) devices constructed from porous materials have been widely studied for the experimental investigation of nanofluidic ion (i.e., nanoionic) transport at the sub–1-nm scale dimension to achieve the ion-specific transport properties observed in biological ion channels (*7*–*9*). For instance, carbon nanotubes (CNTs), graphene, polymers, and metal-organic frameworks (MOFs) have been used to construct nanometer-sized pores to mimic atomic-scale ionic and molecular transport of biological ion channels (*10*–*18*). The promising ion transport properties analogous to biological ion channels such as ultrafast ion transport, high ion-ion selectivity, and quasi-unipolar ion transport have been demonstrated by tuning the effective channel size down to below 1 nm of two-dimensional (2D) layered materials–based (graphene, graphene oxide, $MoS_2$, h-BN, etc.) membranes (*15*, *19*–*21*). Unfortunately, only small ion rectification ratios have been achieved because of the lack of geometry and chemistry diversity along ion transport pathways of these nanoionic devices (*22*, *23*).

The ion rectifying effect (also known as ionic diode behavior) of NCs or membranes has shown important engineering applications. Compared with the nonrectifying ones, the ion-conductive membranes with better ion rectifying property enable higher ion conductance because of the lower transport energy barrier in one direction (*24*, *25*). It is reported that the ion rectifying membranes can suppress power dissipation by blocking the back current, and then improve their energy-harvesting efficiency in reverse electrodialysis (*26*, *27*). The ion rectifying property is normally attributed to the asymmetry in charge density and channel size along the ion transport direction, which has been observed in various heterogeneous NCs or membranes mainly focusing on metal ion rectifying (*17*, *28*). However, rectifying proton transport in NCs/membranes has been rarely reported. Thanks to the tailorable NC diversity in chemistry and geometry of porous framework materials (PFMs), including MOFs and covalent organic frameworks, PFM-based nanofluidic devices have sprung up in recent years, achieving promising ion rectifying properties for sole specie of electrolyte solutions (*29*–*33*). However, the PFM-based NCs reported so far either exhibit low ion conductance or lack ion specificity in ion rectifying. To the best of our knowledge, it remains a challenge to achieve unidirectional transport of metal ions and proton with rectifying direction opposite each other in the same nanoionic channel while having high ion conductance. Since the individual rectifying metal ion conduction or proton conduction is important for many applications such as in energy harvesting and storage and membrane separation, the realization of the dual ion rectifying property would represent a substantial step forward toward the design of more efficient devices in these areas. This kind of exotic ion transport property with integrated multiple functions analogous to the outwardly and inwardly rectifying biological ion channels will inspire more biomimetic design strategies to prepare smart artificial channels/membranes with atomic-scale selective ion transport.

[1]Department of Chemical and Biological Engineering, Monash Center for Membrane Innovation, Monash University, Clayton, Victoria 3800, Australia. [2]CAS Key Laboratory of Mechanical Behavior and Design of Materials; Department of Modern Mechanics, CAS Center for Excellence in Complex System Mechanics, University of Science and Technology of China, Hefei, Anhui 230027, China.
*Corresponding author. Email: huanting.wang@monash.edu (H.W.); wuha@ustc.edu.cn (H.-A.W.)
†These authors contributed equally to this work.

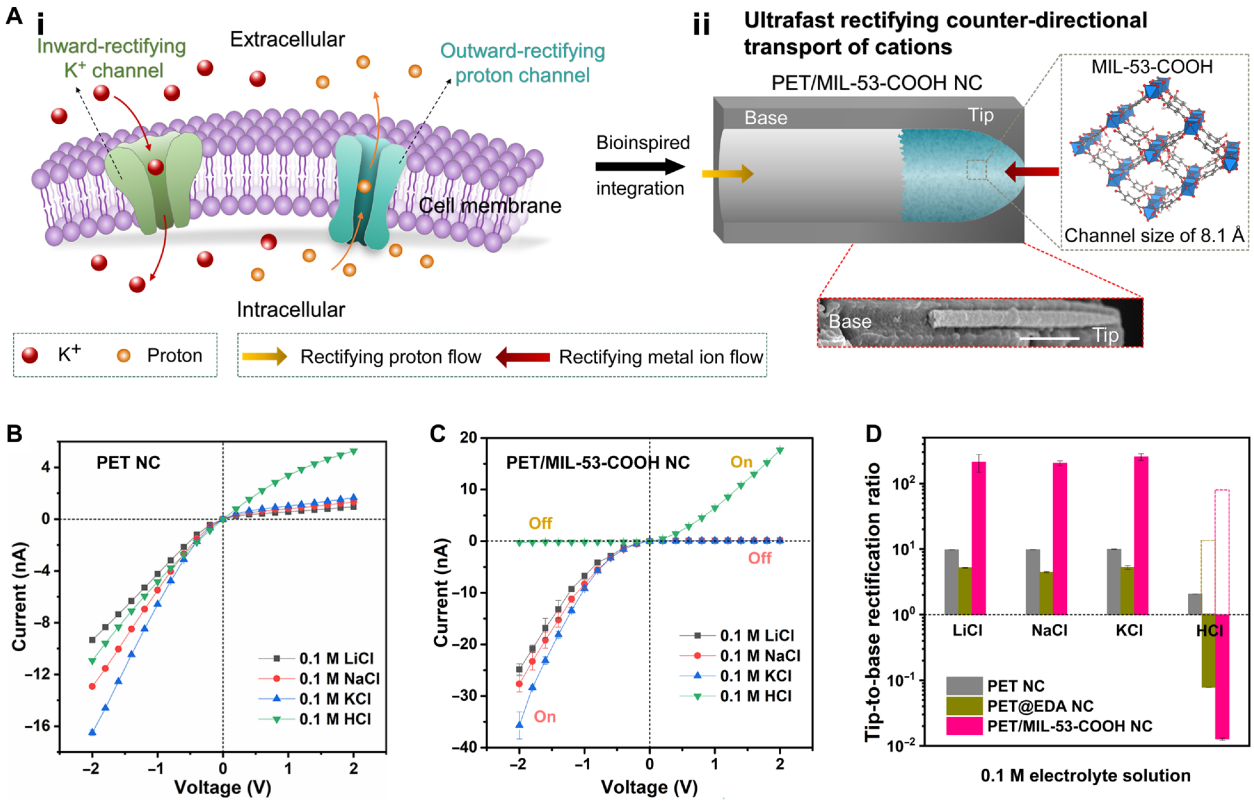


**Fig. 1. Bioinspired design of the MOF nanoionic device for rectifying ultrafast counter-directional transport of metal ions and proton.** (**A**) Bioinspired design of MOF nanoionic device to achieve multifunctional rectifying cation transport. (i) The inward-rectifying $K^+$ channel and outward-rectifying proton channel in cell membrane; (ii) asymmetric PET/MIL-53-COOH NC for counter-directional cation transport. Scanning electron microscopy (SEM) image of the cross section of the PET/MIL-53-COOH NC shows the asymmetric assembly of MOF near the tip side. Scale bar, 1 μm. (**B**) Asymmetrical *I-V* curves of 0.1 M LiCl, NaCl, KCl, and HCl in PET NC. (**C**) Asymmetrical *I-V* curves of 0.1 M LiCl, NaCl, KCl, and HCl in PET/MIL-53-COOH NC. (**D**) The tip-to-base ion rectification ratios in PET/MIL-53-COOH NC compared to those in PET NC and PET@EDA NC. The rectification ratio larger than 1.0 indicates that the preferential cation transport is from the tip to the base side, while the rectification ratio below 1.0 indicates that the preferential cation transport is from the base to the tip side. The dashed columns for HCl are to illustrate the markedly reversed proton rectifying effect of PET@EDA NC and PET/MIL-53-COOH NC compared to the pristine PET NC.

Here, we report a bioinspired artificial ion channel by assembly of acidic MOF (MIL-53-COOH; MIL: Matériaux de l'Institut Lavoisier) into single polyethylene terephthalate NC (PET NC) to achieve ultrafast rectifying counter-directional transport of metal ion and proton. The MIL-53-COOH used in this work has 8.1 Å–sized 1D sub-NCs with high rigidity. This asymmetric PET/MIL-53-COOH NC exhibits the unidirectional proton transport from the base to the tip side, and the preferential metal ion transport from the tip to the base side, both with high ion rectification ratios up to 100. Thus, the proton/metal ion selectivity reaches over 100 with a voltage bias of +2 V. This asymmetric MOF NC has higher metal ion conductance in the tip-to-base direction than the pristine PET NC. The asymmetry of charge density and aperture size from the tip to the base side of the MOF NC is responsible for the metal ion rectifying, as verified by the metal ion concentration profile along the whole channel of MOF NC by finite element method simulations. The PET/MIL-53-COOH NC achieves ultrafast proton permeability, i.e., 4.3 m $s^{-1}$, which is superior to other artificial proton channels. Molecular dynamics (MD) simulations reveal an ultrahigh proton mobility of $11.3 \times 10^{-7}$ $m^2$ /V·s, and further density functional theory (DFT) calculations show that the energy barrier for proton conduction is as low as 0.075 eV in MIL-53-COOH, indicating the ultrafast proton conduction in MOF NC occurs via the Grotthuss mechanism. The energy barrier difference between two transport directions, i.e., 0.08 eV in base-to-tip and 0.18 eV in tip-to-base direction of the MOF NC, explains the high proton rectifying property. As a proof of concept, the PET/MOF nanoionic device is demonstrated as an efficient nanopower generator via reverse electrodialysis, maintaining a stable power density of $10^3$ W/$m^2$ even with the HCl concentration gradient (defined here as the ratio of high to low concentration) decreased to 10. This study demonstrates the rational design of asymmetric nanoionics devices to develop multifunctional biomimetic ion channels and ion-selective membranes for advanced nanofluidics and separation technologies.

## RESULTS

### Preparation of PET/MIL-53-COOH NC

Figure 1A illustrates the biomimetic design of MOF nanoionic device by assembly of rigid MIL-53-COOH with 1D orthorhombic channels into PET NC to achieve ultrafast rectifying counter-directional transport of metal ion and proton. First, we synthesized rigid MIL-53-COOH nanocrystals. The ligand salt–induced MOF nucleation strategy (*34*) was successfully explored for the aqueous phase

synthesis of MIL-53-COOH nanocrystals at 100°C (Supplementary Materials), which was tailored for the subsequent preparation of PET/MOF NC. The deprotonated ligand (1, 2, 4-benzenetricarboxylic acid) favors their coordination bonding with Al-oxide clusters at this moderate temperature and then facilitates the nucleation of MIL-53-COOH. The MIL-53-COOH nanocrystals synthesized were nanoplates with lateral size of about 150 nm and had high crystallinity with featured powder x-ray diffraction (PXRD) peaks of MIL-53-COOH with large-pore (lp) structure (fig. S1, A and B), different with the MIL-53-COOH with narrow-pore structure (*35*, *36*). Notably, the PXRD pattern of MIL-53-COOH in wetting state was the same as that of MIL-53-COOH in dry state (fig. S1B), indicating the low flexibility of the MOF crystal structure. By contrast, the obvious differences were observed in flexible MIL-53–type MOFs between hydrous and anhydrous states, as widely reported in the literature (*36*–*38*). This demonstrates that the framework of the MIL-53-COOH synthesized by this ligand salt–induced strategy exhibits good rigidity. The channels of the as-prepared MIL-53-COOH are free of ligand molecules as confirmed by thermogravimetric analysis (TGA) (fig. S1C) in comparison with the literature data (*34*, *36*). The rigid lp-MIL-53-COOH has ~8.1 Å–sized 1D channels, as indicated by the $N_2$ sorption measurement results (fig. S2).

On the basis of this synthesis method, we fabricated the PET/MIL-53-COOH NC by asymmetric growth of MOF crystals in a bullet-shaped PET NC via nanoconfined assembly strategy (fig. S3 and Materials and Methods). The PET@EDA NC was obtained by modification of PET NC by ethylenediamine (EDA) solution. Note that the bullet shape of the PET NC was key to achieving the asymmetry in the resultant PET/MOF NC device (*30*). The introduction of amino groups dangling in the inner channel wall of PET NC promoted nanoconfined growth of MIL-53-COOH into PET@EDA NC. Scanning electron microscopy (SEM) images and energy-dispersive x-ray spectroscopy mapping images (Fig. 1A-ii insert and fig. S4, A and B) of the cross section of the resulting PET/MOF NC show that the PET channel was filled with well-intergrown MIL-53-COOH crystals several micrometers in length at the tip-side region, leaving the remaining portion unfilled, thus forming an asymmetrical channel structure. Both the bottleneck effect of the tip side and difference in diffusion rate between the ligand ($H_3BTeC$) molecules and $Al^{3+}$ ions favored this asymmetric growth of MOF near the tip side of PET@EDA NC. The PXRD pattern and Fourier transform infrared spectrum show the characteristic peaks and carboxylic-Al-oxide node from MIL-53-COOH, respectively (fig. S4, C and D), further confirming the successful growth of MIL-53-COOH in PET@EDA NC. We recorded the current-voltage (*I-V*) curves for 0.1 M KCl and $MgCl_2$ (fig. S5). On the basis of the conductance at +2 V, the $K^+/Mg^{2+}$ selectivity by PET/MIL-53-COOH NC was up to 49.2, which can be attributed to the size sieving effect of the MOF intrinsic channels (8.1 Å) as the cutoff for $Mg^{2+}$ (8.56 Å) and $K^+$ (6.66 Å). This good ion selectivity together with the SEM image (Fig. 1A-ii) can qualitatively demonstrate the well intergrowth of MOF crystals in the tip-side region of PET/MIL-53-COOH NC.

## Rectifying counter-directional transport of metal ions and proton

The *I-V* characteristic curves were measured in 0.1 M LiCl, NaCl, KCl, and HCl for the PET/MOF NC, PET NC, and PET@EDA NC (Fig. 1, B and C, and fig. S6A). In contrast with PET NC, the PET/MIL-53-COOH NC presented the "on" state for metal ions ($Li^+$, $Na^+$, and $K^+$) when a forward voltage was applied to the tip side (set as a negative voltage), and the "off" state with a forward voltage applied to the base side (set as a positive voltage); it exhibited the reversed rectifying transport for the proton conduction. This transport behavior for alkaline metal ions and proton mimics counter-directional transport properties of cell membranes composed of both inwardly rectifying potassium ion channels (*6*, *39*) and outwardly rectifying proton channels (*40*–*42*). To further demonstrate this distinct cation rectifying effect, we calculated ion rectification ratios (Fig. 1D). Here, the ion rectification ratio in the tip-to-base direction is defined as the absolute ratio of the currents at negative voltage over positive voltage, i.e., $\left| I_{-2V}/I_{+2V} \right|$. This tip-to-base rectification ratio larger than 1.0 indicates that the preferential cation transport is in the tip-to-base direction, whereas the lower rectification ratio below 1.0 means the preferential cation transport is in the base-to-tip direction. Conversely, the base-to-tip rectification ratio is defined by $\left| I_{+2V}/I_{-2V} \right|$ to demonstrate the degree of ion rectifying effect on the opposite direction of proton transport through the NCs. Our measurements showed that the tip-to-base rectification ratios for LiCl, NaCl, and KCl in PET/MIL-53-COOH NC were in the range of 205 to 255, over 20 times higher than those for pristine PET NC. However, the proton conduction was opposite. The PET NC had a weak rectifying effect for HCl in the tip-to-base direction with a low rectification ratio of 2.5. In contrast, the preferential proton transport was reversed to the base-to-tip direction after amino group modification, and this reversed rectifying effect for HCl was further enhanced in PET/MIL-53-COOH NC, with the rectification ratio decreasing from 0.07 to 0.013. In other words, the proton rectification ratio in the base-to-tip direction increased from 18 in PET@EDA NC to 78.5 in PET/MIL-53-COOH NC, about 7.2 and 32 times higher than that in PET NC, respectively, as shown in Fig. 1D. The ideal cation selectivity was calculated by taking the ratio of the currents of different cations at a voltage of +2 V (fig. S6B). The PET/MIL-53-COOH NC exhibited high proton/metal ion selectivity, with the ideal $H^+/Li^+$, $H^+/Na^+$, and $H^+/K^+$ selectivity of 100, over 50 times higher than those in PET NC; it had binary proton/metal ion selectivity of between 23 and 60 based on the ion permeation experiments (Supplementary Materials). These values are listed in table S1 in comparison with biological channels and previously reported artificial proton channels.

The comparison of metal ion conductance is shown in Fig. 2A, and the PET/MIL-53-COOH NC exhibits improved metal ion conductance, around two times higher than that in pristine PET NC at −2 V, which shows a notable contrast with lower ion conductance of previous MOF NCs than that of PET NC (*30*, *43*, *44*). The improved metal ion conductance in PET/MIL-53-COOH NC is attributed to the enriched ion concentration and the enhanced metal ion mobility in MOF sub-NCs; for example, $K^+$ mobility is up to $8.4 \times 10^{-8}$ $m^2/V{\cdot}s$ in MIL-53-COOH 1D sub-NCs by MD simulations (fig. S7) versus $7.6 \times 10^{-8}$ $m^2/V{\cdot}s$ in the bulk (*45*). To further demonstrate this ultrafast and unidirectional metal ion transport in PET/MIL-53-COOH NC, we obtained the *I-V* curves of LiCl, NaCl, and KCl at different concentrations (fig. S8). The conductance in two opposite directions (at −2 V and +2 V) both increased with increasing the concentration (Fig. 2B). As demonstrated in Fig. 2C, the PET/MIL-53-COOH NC showed robust rectifying effect for the metal ions. Specifically, the metal ion–rectification ratio maintained over 100 as the concentration increased from 1 mM to 0.1 M and reduced to ~50 with the concentration increasing to 1.0 M. This

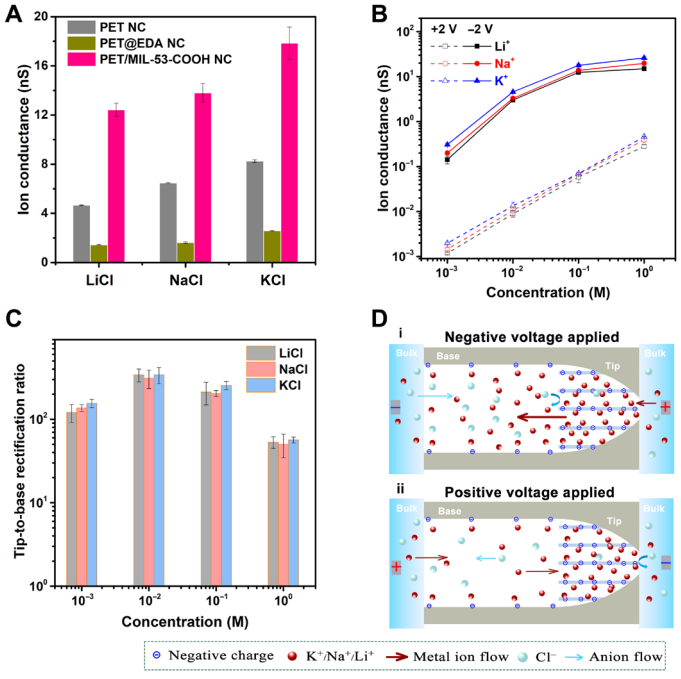


**Fig. 2. Ultrafast, unidirectional metal ion transport in PET/MIL-53-COOH NC.** (**A**) Comparison of 0.1 M KCl, NaCl, and LiCl conductance in PET NC before and after EDA and MOF modification. (**B**) Conductance of KCl, NaCl, and LiCl in PET/MIL-53-COOH NC as a function of electrolyte concentration. (**C**) Ion rectification ratio (tip-to-base) for LiCl, NaCl, and KCl with the variation of electrolyte concentration. (**D**) Schematic of ion rectification mechanism for metal ions in PET/MIL-53-COOH NC. (i) Enhanced ion conduction at negative voltage applied; (ii) low ion conduction at positive voltage applied.

metal ion rectifying property is attributed to the enhanced asymmetry in channel size and charge density between the tip and base sides of PET/MIL-53-COOH NC, compared to the pristine PET NC. These asymmetries can be quantitatively described by the base/tip ratio of channel size and tip/base ratio of negatively charged density, respectively. Specifically, the channel size asymmetry increased markedly from 6.1 for PET NC and PET@EDA NC to 432 for PET/MIL-53-COOH NC (fig. S9). Furthermore, the PET/MIL-53-COOH NC was negatively charged in these chloride salt solutions because of the deprotonation of free -COOH groups, as confirmed by the minus zeta potential of MIL-53-COOH (table S2). The charge density asymmetry increased to 8.6 for PET/MIL-53-COOH NC, while there was no charge asymmetry for PET NC and PET@EDA NC (figs. S10 and S11). The increased asymmetry in both channel size and charge density (details seen in the Supplementary Materials) greatly contributed to high rectification ratios of chloride salt solutions in PET/MIL-53-COOH NC.

Our drift-diffusion experiments showed that the cation transfer number for KCl was 0.943, corresponding to a $K^+/Cl^-$ selectivity of 16.4, indicating that PET/MIL-53-COOH NC has a good cation/anion charge selectivity (table S3), and the metal ions play a major role in charge transfer. In general, the metal ions of smaller hydrated diameters than the MOF channel size (i.e., $K^+$ 6.62 Å, $Na^+$ 7.16 Å, and $Li^+$ 7.64 Å versus ~8.1 Å) are favorably enriched in the negatively charged PET/MIL-53-COOH NC, while the counter ion ($Cl^-$) is depleted. Since MOF channels have higher negative charge density than the non–MOF-filled NC zone at the base side (−1.8 e/nm$^2$ versus −0.23 e/nm$^2$), the electrostatic attraction induced much higher metal ion concentration in the tip zone and slightly increased metal ion concentration than bulk in the non–MOF-filled NC zone, thus resulting in a concentration gradient in the tip-to-base direction in PET/MIL-53-COOH NC. When a negative voltage bias was applied, i.e., the forward voltage applied to the tip side, the electrokinetic metal ion transport follows the ion concentration gradient, producing enhanced ion flux (Fig. 2D-i). Furthermore, the anions can transfer from the bulk solution into the base side of PET/MIL-53-COOH NC, but they cannot pass through the MOF sub-NCs at the tip side because of the electrostatic repulsion of the overlapped electric double layers in MOF sub-NCs. This results in the accumulated anions at the base side of PET/MIL-53-COOH NC. To balance the excessive anions at the base side, more metal ions need to transfer to the base side from the MOF channels. As a result, the metal ions and anions are enriched at the non–MOF-covered base side compared to the condition without voltage applied. The metal ion transport follows the concentration gradient and the ion enrichment effect. These effects synergistically favor the enhanced ionic current generated with a negative voltage applied. However, there is a different case with a positive voltage applied, i.e., the forward voltage applied at the base side. In this case, the metal ions transfer from the base side to the tip side against the ion concentration gradient in PET/MIL-53-COOH NC, compromising the metal ion flux, and thus producing low current (Fig. 2D-ii). Meanwhile, the anions transport from the base side to the bulk solution but without anion offset from the tip side because of the high electrostatic repulsion of MOF channels. In the end, both the metal ions and anions are depleted in the non–MOF-covered base, compared to the condition without voltage applied. Both the metal ion transport against the concentration gradient and ion depletion finally lead to the low current with positive voltage applied. The metal ion concentration profile in PET/MIL-53-COOH NC was further evaluated by using the numerical simulation based on the Poisson and Nernst-Planck equations (Supplementary Materials). A 3D model with channel size and charge density similar to the PET/MIL-53-COOH NC was established as shown in fig. S12, which helps explain the metal ion rectifying transport in the PET/MIL-53-COOH NC. The ion concentration profiles calculated at voltage bias of −2, 0, and +2 V (figs. S13 and S14) illustrate the metal ion accumulation and depletion effect under negative and positive voltage bias, respectively. The simulation results showed that the metal ion concentration in the tip side of the PET/MIL-53-COOH NC was almost the same no matter what voltage was applied (fig. S14A), because the highly negatively charged MOF sub-NCs attracted metal ions via electrostatic interaction.

We further tested *I-V* curves of HCl at different concentrations (fig. S15) and calculated the base-to-tip rectification ratio (Fig. 3A). The proton rectification ratio maintained at over 80 as the HCl concentration increased from 0.01 to 0.1 M and dropped to ~10 at a high concentration of 1.0 M. Notably, the HCl conductance at +2 V in the PET/MIL-53-COOH NC was 100 times higher than that in the pristine PET NC and even higher than that in the PET@EDA NC (Fig. 3B). The ion permeation experiments were performed. The pH value at the permeate side of PET/MIL-53-COOH NC decreased markedly as opposed to a slight decrease in PET NC (Fig. 3C), with a proton permeability of 4.3 m/s versus $1.5 \times 10^{-2}$ m/s. Furthermore, the proton transfer number (indicator of the proton/$Cl^-$ selectivity) of different NCs studied was determined by drift-diffusion experiments (fig. S16 and table S3), with the transfer number of CNTs

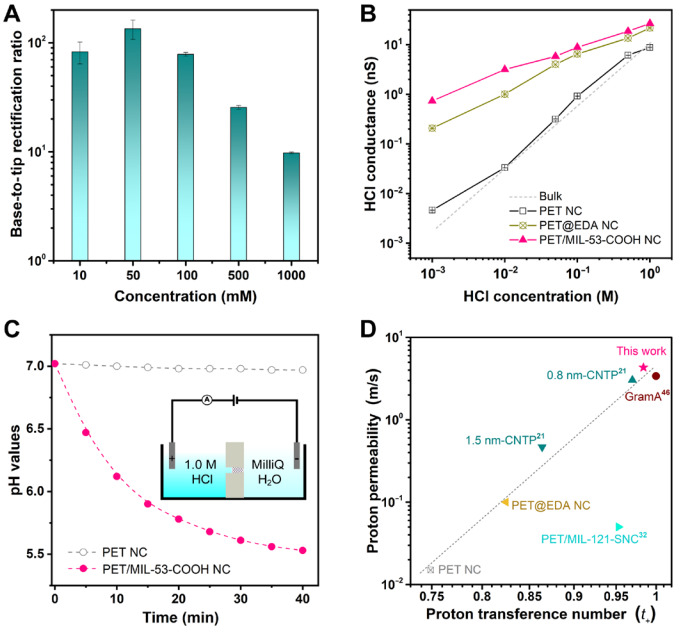


**Fig. 3. Ultrafast, unidirectional proton transport in PET/MIL-53-COOH NC.** (**A**) Base-to-tip rectification ratio for HCl as a function of electrolyte concentration. (**B**) The HCl conductance as a function of concentration in PET NC, PET@EDA NC, and PET/MIL-53-COOH NC compared to bulk HCl values. (**C**) The variation of pH value on the permeate side as a function of time for PET/MIL-53-COOH NC and PET NC. The insert is the schematic diagram showing the ion permeation experiment with a voltage bias of 1.0 V. (**D**) The proton permeability of different artificial proton channels in comparison with biological proton channel (GramA) with their respective proton transference number. The PET/MIL-53-COOH NC exhibits high proton permeability and charge selectivity compared to other artificial and biological proton channels.

calculated by simulations (Supplementary Materials), all compared in Fig. 3D. It shows that the PET/MIL-53-COOH NC functions as an outstanding biomimetic proton channel comparable to proton channels (GramA) (*46*) in terms of both proton permeability and charge selectivity, exceeding previous artificial channels (*21*, *32*). This ultrahigh proton permeability is presumably related to the rigid 1D NCs with orthorhombic geometry of MIL-53-COOH, compared to the monoclinic channels of MIL-121.

## Ultrafast rectifying proton transport mechanisms

To reveal the ultrafast proton transport mechanism at the molecular level, comprehensive theoretical simulations were conducted (Materials and Methods and Supplementary Materials). We firstly established a simulation model (fig. S17) to investigate the water configuration in the 8.1 Å–sized 1D channel of MIL-53-COOH. The results showed that the highly ordered arrangement of water molecule clusters in MOF NC (Fig. 4, B and C) was formed under the subnanoscale confinement effect, which was key to fast proton conduction. Moreover, the polarity sites, including bridging oxygen (O1), carbonyl oxygen (O2), and hydroxyl oxygen (O3) (Fig. 4A), facilitated the formation of cooperative hydrogen bond networks between water chains and MIL-53-COOH walls, and then the highly ordered arrangement of water molecule clusters in the MOF channels (Fig. 4, B and C), which provided a more effective medium for proton conduction. The water molecules near the polarity sites of MOF walls were substantially activated by the strong local electronic field (Fig. 4, D-i and ii), in which the spatial structure (bond length) and Bader charge distribution of water molecules changed notably upon approaching the polarity sites of MOF walls (Fig. 4E and fig. S18). Meanwhile, the statistical analysis of the radial density profiles (Fig. 4D-iii) indicates that most of the water molecules closely approach polarity sites (< 3 Å). As a result, these polarized water molecules more easily engender the breaking and bonding behavior in hydrogen bonds, consequently facilitating proton movement between water molecules and promoting the Grotthuss conduction in MIL-53-COOH channels. We further quantitatively investigated the ultrafast proton conduction by calculating the proton mobility with voltage applied in the longitudinal direction of the 1D channels of the MOF (fig. S19). The proton mobility in other artificial NCs including 0.8-nm CNT, 1.5-nm CNT, and MIL-121 was also compared (Fig. 4F). As shown in Fig. 4G, the MIL-53-COOH displays the outstanding proton mobility of $11.3 \times 10^{-7}$ $m^2$ /V·s, superior to other previous artificial proton channels such as the 0.8-nm CNT with ultrafast proton conduction (*21*).

The mechanism of the ultrafast rectifying proton conduction in the asymmetric PET/MIL-53-COOH NC was investigated from the perspective of the arrangement of water clusters in the MOF-filled zone. Figure S20 shows that the water molecules in the MOF sub-NCs have the preferential orientation when rushing from the bulk solution to the MOF sub-NCs, and this specific water configuration features an orientation angle (θ) below 90° for water molecules that are marked in red color (i.e., following the base-to-tip side direction). They can maintain this specific orientation under a wide range of electric fields including the applied voltage bias in the experiments (fig. S20B). We have further established the bullet-shaped pore network model to simulate the effect of the bulk water from both side reservoirs on the water configuration in the MOF-filled zone in PET/MIL-53-COOH NC, as shown in fig. S21. Since the pore mouth area of the base side is more than 36 times larger than that of the tip side, most of the water molecules in the MOF-filled zone of the PET/MIL-53-COOH NC come from the bulk solution in the base side reservoir and have the orientation angle of below 90° (i.e., base-to-tip direction), while only a small proportion of water in the local tip size have the orientation angle of above 90° (i.e., tip-to-base direction) as illustrated by the vast red area compared to the blue area in fig. S21 (A and B). To maintain the stability of the system, the water molecules in the MOF-filled zone at the tip side with the opposite orientation will gradually reverse their orientations to achieve orientation consistence for almost all water molecules in MOF sub-NCs (fig. S21, C and D). Consequently, the DFT calculations prove that the MIL-53-COOH NC exhibits an ultralow energy barrier (0.08 eV) for proton conduction in the base-to-tip direction, but a higher energy barrier (0.18 eV) in the opposite tip-to-base direction (Fig. 4H), which is close to that in bulk water (~0.21 eV; fig. S22, A and B). Furthermore, in the base-to-tip direction, three polarity sites (O1 to O3 in Fig. 4A) facilitate proton hopping transport along the MIL-53-COOH 1D sub-NCs by reducing its energy barrier. As shown in fig. S22, the energy barriers near polarity sites (i.e., 0.017 to 0.082 eV; fig. S22, C to H) are much lower than that at the middle region of MOF channels (i.e., 0.155 eV; fig. S22, I and J). However, in the opposite direction, the energy barrier increases to 0.152 to 0.361 eV (fig. S22, D, F, H, and J). This indicates that the polarization effect can substantially reduce the energy barrier, resulting in ultrafast proton hopping transport in

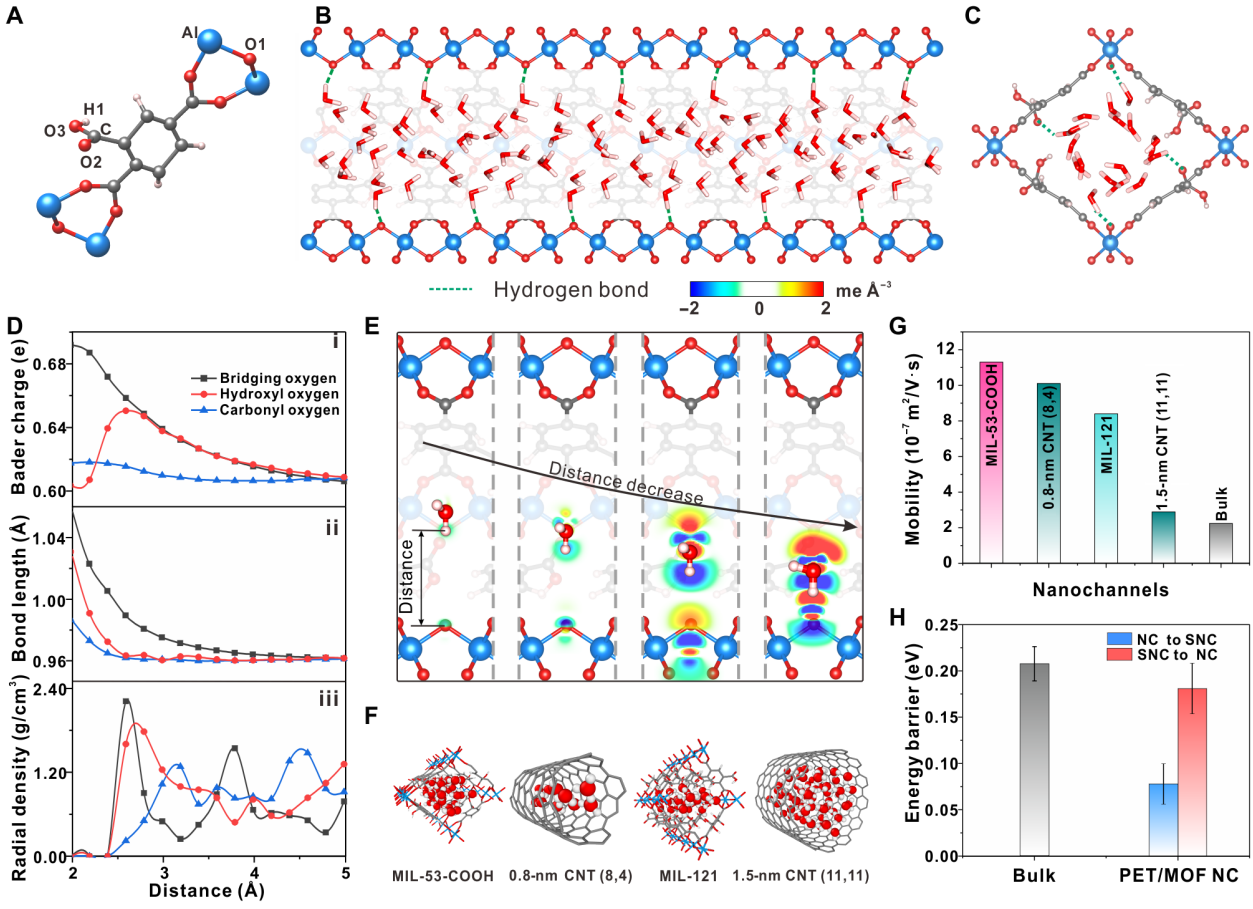


**Fig. 4. Theoretical simulations revealing the mechanisms for ultrafast proton transport in PET/MIL-53-COOH NC.** (**A**) Basic molecular structure of MIL-53-COOH to highlight the polarity sites [bridging oxygen (O1), carbonyl oxygen (O2), and hydroxyl oxygen (O3)]. (**B** and **C**) The structural characteristic of water molecule chains confined in MIL-53-COOH sub-NCs, where the front view (B) shows the water configuration along the axial direction of the MOF sub-NC, and the side view (C) is the representative slice along the radial direction. The water chain in MIL-53-COOH is constructed under the hydrogen bonds effect between the water molecules and the polarity sites of MOF channel walls. (**D**) The Bader charge of hydrogen atoms (i) and hydrogen-oxygen bond length (ii) in water molecules as a function of the distance between water and MOF polarity sites, as well as the radial density distribution (iii) between water molecules and MOF polarity sites. (**E**) The contour map of differential charge density of the water molecules upon approaching the polarity bridging oxygen sites in MOF walls. (**F** and **G**) Configurations of water chains confined in various artificial proton channels and their corresponding proton mobility, including MIL-53-COOH, MIL-121, and CNTs with sizes of 0.8 nm (8, 4) and 1.5 nm (11, 11), and the proton mobility in bulk water is introduced as the benchmark. (**H**) The energy barrier of proton transport in MIL-53-COOH channels in two opposite directions, indicating the proton rectifying and ultrafast proton conduction, with the higher energy barrier in bulk water as a reference. Note that NC stands for the non–MOF-filled zone of the PET/MIL-53-COOH NC, and SNC stands for the MOF sub-NC.

MIL-53-COOH. Therefore, the overall energy barriers of proton conduction signify ultrafast and unidirectional transport properties of the PET/MIL-53-COOH NC because they determine the ion transport rate in the NCs (*47*).

The zeta potential of the MIL-53-COOH particle was measured to be from 25.4 to 37.5 mV in HCl solution with a concentration range of 0.01 to 1.0 M, indicating that the MOF sub-NCs are positively charged in the HCl solution in our experiments. Like the case of metal ions, the proton interaction with the positively charged NC and MOF sub-NCs may cause the proton concentration gradient in the base-to-tip side direction, which also favors the preferential proton transport in the base-to-tip direction to some extent. In conclusion, ultrafast rectifying proton conduction is attributed to greatly enhanced Grotthuss mechanism by highly ordered water clusters, polarity sites induced polarized water molecules in MOF sub-NCs and asymmetric porous structure of PET/MIL-53-COOH NC.

## Application of MOF NC for osmotic power harvesting

Considering the ultrafast proton conduction and superior proton/$Cl^-$ selectivity, we also explored the potential of the PET/MIL-53-COOH NC as a nanopower generator to harvest the osmotic energy from HCl concentration gradient in reverse electrodialysis. The diffusion potential ($V_{os}$) and osmotic current ($I_{os}$) were obtained from *I-V* curves with concentration gradient from 10 to 1000 (Fig. 5, A and B). As shown in Fig. 5C, the osmotic current density increased markedly from $4.71 \times 10^3$ to $1.95 \times 10^5$ A/m$^2$, and the diffusion potential increased steadily from 57.3 to 65.1 mV, with increasing HCl concentration bias across the PET/MIL-53-COOH NC. As a result, the power density of PET/MIL-53-COOH NC was 67.4, 445.1, 1640.9, and 3174.3 W/m$^2$ with the concentration bias of 10, 100, 500, and 1000, respectively (Fig. 5D). This osmotic power level is among of the highest values obtained previously in polymer solid-state NCs and 2D laminar nanopower generators (tables S5 and S6).

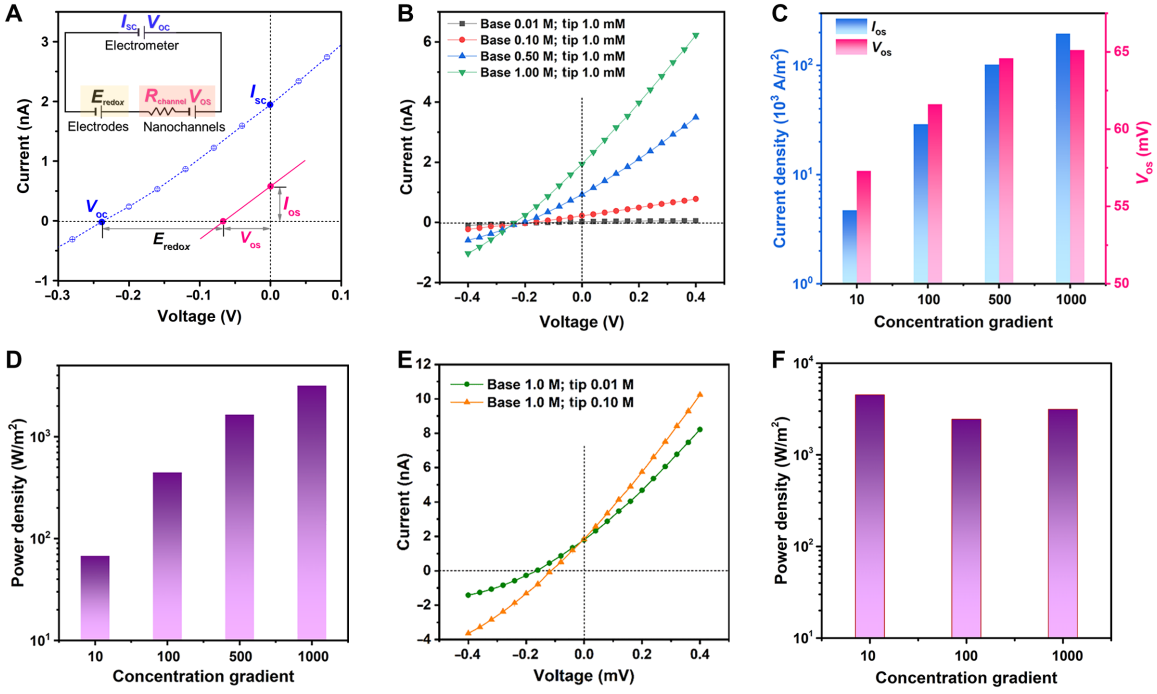


**Fig. 5. Osmotic power generation by the PET/MIL-53-COOH NC.** (**A**) Typical *I-V* curves under a 100-fold HCl gradient (base side 1.0 M/tip side 0.01 M). The insert diagram shows the contributions of different parts of the system to the overall measured voltage. The short-circuit current ($I_{sc}$) and open-circuit voltage ($V_{oc}$) can be obtained from the observed intercepts on the current axis and voltage axis, respectively. The pure osmotic power contribution (red line) can be evaluated from the original total current by subtracting the contribution of the redox potential ($E_{redox}$) on the Ag/AgCl electrodes. $V_{os}$ and $I_{os}$ are the diffusion potential and osmotic current, respectively. (**B**) *I-V* curves of HCl under different concentration gradient across the PET/MIL-53-COOH NC. (**C**) Generated osmotic current density and diffusion potential as a function of HCl concentration gradient. (**D**) Output osmotic power density as a function of HCl concentration gradient. (**E**) *I-V* curves measured with 0.1 and 0.01 M HCl on the low concentration side. (**F**) Power density as a function of concentration gradient with the HCl concentration of the base side set as 1.0 M.

The cycling osmotic power generation performance is shown in fig. S24, demonstrating that PET/MIL-53-COOH NC has good performance stability. The osmotic current stayed at high level with the concentration gradient reduced to even 10 when the HCl concentration on the high concentration side was fixed as 1.0 M (Fig. 5E). As a result, the output power density reached up to 4509 W/m$^2$ with a concentration gradient of 10 (Fig. 5F). These results demonstrate that the PET/MIL-53-COOH NC can effectively function as the nanopower generator via reverse electrodialysis.

## DISCUSSION

In summary, we demonstrate that an MOF nanoionic device (PET/MIL-53-COOH NC) exhibits rectifying metal ion and proton transport with respective ultrahigh conduction in the opposite directions. Comprehensive theoretical simulations reveal the ultrahigh proton mobility and low energy barrier in the 1D MOF sub-NCs, which explains the ultrahigh proton permeability of the PET/MIL-53-COOH NC superior to previously reported artificial proton channels. Different from the metal ion rectifying effect that stems from the asymmetry in charge and channel size between the tip and base sides, the unidirectional proton transport is governed by the energy barrier difference for entry into or exit out of the MIL-53-COOH sub-NCs within the PET/MOF NC. In addition, as a nanopower generator, the PET/MIL-53-COOH NC exhibits outstanding output power density in the reverse electrodialysis process. In contrast with previously reported nanopower generators that often suffer from obviously decreased power density with decreasing concentration gradient (*48*, *49*), this MOF nanoionic device maintains a stable output power density with a concentration gradient as low as 10 at the constant high concentration. These results indicate that the MOF nanoionic device has advantage in achieving high energy efficiency in osmotic power harvesting (*26*, *50*). Considering the high proton/metal ion selectivity, this MOF NC system shows great application potential in an integrated process of osmotic power harvesting and acidic recovery in many industries (*51*, *52*).

Our work demonstrates that biomimetic ion regulation with atomic-scale precision analogous to the core functions of biological ion channels can be realized by rational design of heterogeneous MOF NCs. More bioinspired nanofluidic devices with integrated functions are expected to emerge in the near future, considering the increasing number and functional structures of PFMs available.

## MATERIALS AND METHODS

### Chemicals and materials

Aluminum chloride hexahydrate ($AlCl3{\cdot}6H_2O$), 1,2,4-benzenetricarboxylic acid (H3BTeC), potassium chloride (KCl), sodium chloride (NaCl), lithium chloride (LiCl), hydrochloric acid (HCl), 2-(*N*-morpholino) ethanesulfonic acid (MES), *N*-(3-dimethylaminopropyl)-*N*′-ethylcarbodiimide hydrochloride (EDC), and *N*-hydroxysulfosuccinimide sodium salt (NHSS), were purchased from Sigma-Aldrich, Australia. Methanol and NaOH were purchased

from Merck. PET films were provided by GSI Helmholtz Centre (Darmstadt, Germany).

### Preparation of PET/MIL-53-COOH NC

A nanoconfined interfacial growth strategy was used to assemble MIL-53-COOH nanocrystals into the single bullet-shaped PET@EDA NC. The PET@EDA NC was prepared by modifying our previous method (*44*). The PET@EDA NC film was clamped within the homemade interfacial synthesis device with two cells. A total of 0.70 g of 1, 2, 4-benzenetricarboxylic acid and 0.345 g of NaOH were dissolved in 5 ml of Milli-Q $H_2O$ (as solution A), and 1.12 g of $AlCl_3{\cdot}6H_2O$ was dissolved in 5 ml of Milli-Q $H_2O$ (as solution B). Both solutions A and B were preheated to 90°C by a hotplate and then quickly added to the cell facing the tip and base sides of the PET@EDA NC, respectively. Afterward, the device was sealed into a polytetrafluoroethylene (PTFE)–lined autoclave and then transferred into an oven preheated to 100°C and maintained at this temperature for 48 hours under static condition. After the oven cooled to room temperature, the MOF modified PET@EDA NC film was taken out, washed thoroughly with distilled water, and finally dried at room temperature.

### Electrochemical measurements

The ionic transport properties of PET NC, PET@EDA NC, and PET/MOF NC were studied by recording *I-V* curves with Keithley 6487 and 6517B picoammeters. These single NCs were clapped between two chambers that were filled with individual chloride salt solution (i.e., KCl, NaCl, or LiCl with pH 5.8) or HCl solutions at the same concentration. The pH values of KCl, NaCl, and LiCl solutions were adjusted by adding a tiny amount of hydroxide salt (i.e., KOH, NaOH, and LiOH, respectively) together with HCl. The Ag/AgCl electrodes were used to apply a transmembrane potential. The anode was placed in the chamber facing the base side of the NC membranes. The main transmembrane potential used in this work was a scanning voltage that varied from −2 to +2 V. In this work, each *I-V* measurement was repeated at least three times to obtain the average current at specific voltage bias applied.

### Ion rectification ratio

The ion rectification ratio was calculated as the absolute current ratio of a given positive voltage bias over a negative voltage bias (that is, $I_{+2V}$ versus $I_{-2V}$). For quantitative compar ison of the unidirectional cation transport, the tip-to-base rectification ratio of chloride electrolyte solutions is defined as $\left| I_{-2V}/I_{+2V} \right|$, while the base-to-tip rectification ratio is defined as $\left| I_{+2V}/I_{-2V} \right|$.

### Ion permeation experiments

Ion permeation experiments were conducted to determine the proton permeability by NCs (including PET NC, PET@EDA NC, and PET/MOF NC). The PET film–embedded NCs were clipped between two PTFE cells, one of which was filled with 1.0 M HCl as the feed side and the other with Milli-Q water as the permeate side (Fig. 3C, inset). The solutions at both sides were stirred to minimize the effect of ion concentration polarization. The pH meter was inserted into the permeate side to detect the variation of pH value with time.

### Finite element method simulations

To study the metal ion rectifying mechanism, a 3D model was constructed to simulate the electro-kinetic metal ion transport inside the PET/MIL-53-COOH NC based on the Poisson-Nernst-Planck equation using COMSOL multiphysics solver (*53*, *54*), as shown in fig. S12. Compared to that with no voltage bias applied, the $K^+$ concentration in the left nanospace greatly increased with negative voltage bias and depleted with positive voltage bias (figs. S13 and S14), which is consistent with the proposed rectifying mechanism for metal ions in the PET/MIL-53-COOH NC. The detailed simulation process can be seen in the Supplementary Materials.

### MD simulations

The MD simulations were performed to reveal water chain structures within MIL-53-COOH channels and its proton conduction properties. The MIL-53-COOH unit cell used in this work is illustrated in fig. S17A. Then, the 6 × 6 × 30 periodic supercell of MOF was constructed on the basis of its unit cell, and one representative cell was selected to build the MOF channel with an axial length of about 150 Å. The detailed water chain configurations are shown in fig. S17 (C and D). This series of simulations were performed in the classic Dreiding force field (*55*). The proton conduction mobility was subsequently estimated on the basis of the obtained water chain structures, as shown in fig. S17 (E and F), where the force field is the reactive force field that has been proven as an effective force field to describe the bond breaking and forming (*56*). We also calculated the proton mobility in MIL-121, 0.8-nm CNT and 1.5-nm CNT to correlate their mobility with the proton permeability by the respective artificial proton channel (details seen in the Supplementary Materials). The structure details of MIL-53-COOH and MIL-121 in simulations are shown in table S4. All the MD simulations were performed with a Large-scale Atomic/Molecular Massively Parallel Simulator (LAMMPS) program (*57*).

### DFT calculations

DFT calculations were used to evaluate the differential charge density and the energy barrier during the proton conduction process within MOF channels, as shown in figs. S18 and S22. Initial models were extracted from the above MD simulations, with a 1 × 1 × 2 representative periodic supercell of MIL-53-COOH. The charge transfer between water molecules and polarity sites in MOF walls was quantitatively revealed by differential charge density calculations, indicating the activation state of water molecules for higher proton conduction capacity (Fig. 4, D and E). The energy barrier was quantified by the climbing image nudged elastic band method (*58*) to reflect the difficulty of proton conduction from the energy perspective. The results showed that the proton conduction within MOF channels was much easier than that in bulk water system and manifested a typically unidirectional conduction feature. This proved the fast and unidirectional proton conduction characteristic of PET/MIL-53-COOH NC. All DFT calculations were performed in the Quantum Espresso package (*59*) based on the generalized-gradient approximation with the functional of Perdew-Burke-Ernzerhof (*60*).

## SUPPLEMENTARY MATERIALS

Supplementary material for this article is available at https://science.org/doi/10.1126/sciadv.abl5070

## REFERENCES AND NOTES

1. W. A. Catterall, Structure and function of voltage-sensitive ion channels. *Science* **242**, 50–61 (1988).
2. D. A. Doyle, J. M. Cabral, R. A. Pfuetzner, A. Kuo, J. M. Gulbis, S. L. Cohen, B. T. Chait, R. MacKinnon, The structure of the potassium channel: Molecular basis of $K^+$ conduction and selectivity. *Science* **280**, 69–77 (1998).

3. R. MacKinnon, Potassium channels and the atomic basis of selective ion conduction (Nobel Lecture). *Angew. Chem. Int. Ed.* **43**, 4265–4277 (2004).
4. E. Gouaux, R. MacKinnon, Principles of selective ion transport in channels and pumps. *Science* **310**, 1461–1465 (2005).
5. T. Dudev, C. Lim, Ion selectivity strategies of sodium channel selectivity filters. *Acc. Chem. Res.* **47**, 3580–3587 (2014).
6. H. Hibino, A. Inanobe, K. Furutani, S. Murakami, I. Findlay, Y. Kurachi, Inwardly rectifying potassium channels: Their structure, function, and physiological roles. *Physiol. Rev.* **90**, 291–366 (2010).
7. L. Bocquet, Nanofluidics coming of age. *Nat. Mater.* **19**, 254–256 (2020).
8. R. Epsztein, R. M. DuChanois, C. L. Ritt, A. Noy, M. Elimelech, Towards single-species selectivity of membranes with subnanometre pores. *Nat. Nanotechnol.* **15**, 426–436 (2020).
9. J. Gao, Y. Feng, W. Guo, L. Jiang, Nanofluidics in two-dimensional layered materials: Inspirations from nature. *Chem. Soc. Rev.* **46**, 5400–5424 (2017).
10. F. Fornasiero, H. G. Park, J. K. Holt, M. Stadermann, C. P. Grigoropoulos, A. Noy, O. Bakajin, Ion exclusion by sub-2-nm carbon nanotube pores. *Proc. Ntal. Acad. Sci. U.S.A.* **105**, 17250–17255 (2008).
11. B. Radha, A. Esfandiar, F. Wang, A. Rooney, K. Gopinadhan, A. Keerthi, A. Mishchenko, A. Janardanan, P. Blake, L. Fumagalli, M. Lozada-Hidalgo, S. Garaj, S. J. Haigh, I. V. Grigorieva, H. A. Wu, A. K. Geim, Molecular transport through capillaries made with atomic-scale precision. *Nature* **538**, 222–225 (2016).
12. K.-G. Zhou, K. Vasu, C. Cherian, M. Neek-Amal, J. C. Zhang, H. Ghorbanfekr-Kalashami, K. Huang, O. Marshall, V. Kravets, J. Abraham, Y. Su, A. N. Grigorenko, A. Pratt, A. K. Geim, F. M. Peeters, K. S. Novoselov, R. R. Nair, Electrically controlled water permeation through graphene oxide membranes. *Nature* **559**, 236–240 (2018).
13. C. Cheng, G. Jiang, C. J. Garvey, Y. Wang, G. P. Simon, J. Z. Liu, D. Li, Ion transport in complex layered graphene-based membranes with tuneable interlayer spacing. *Sci. Adv.* **2**, e1501272 (2016).
14. J. P. Thiruraman, P. Masih Das, M. Drndić, Ions and water dancing through atom-scale holes: A perspective toward "size zero". *ACS Nano* **14**, 3736–3746 (2020).
15. H. Zhan, Z. Xiong, C. Cheng, Q. Liang, J. Z. Liu, D. Li, Solvation-involved nanoionics: New opportunities from 2D nanomaterial laminar membranes. *Adv. Mater.* **32**, 1904562 (2020).
16. S. Kim, H. Wang, Y. M. Lee, 2D nanosheets and their composite membranes for water, gas, and ion separation. *Angew. Chem. Int. Ed.* **58**, 17512–17527 (2019).
17. W. Guo, Y. Tian, L. Jiang, Asymmetric ion transport through ion-channel-mimetic solid-state nanopores. *Acc. Chem. Res.* **46**, 2834–2846 (2013).
18. J. Lu, H. Wang, Emerging porous framework material-based nanofluidic membranes toward ultimate ion separation. *Matter* **4**, 2810–2830 (2021).
19. J. Abraham, K. S. Vasu, C. D. Williams, K. Gopinadhan, Y. Su, C. T. Cherian, J. Dix, E. Prestat, S. J. Haigh, I. V. Grigorieva, P. Carbone, A. K. Geim, R. R. Nair, Tunable sieving of ions using graphene oxide membranes. *Nat. Nanotechnol.* **12**, 546–550 (2017).
20. A. R. Koltonow, J. Huang, Two-dimensional nanofluidics. *Science* **351**, 1395–1396 (2016).
21. R. H. Tunuguntla, F. I. Allen, K. Kim, A. Belliveau, A. Noy, Ultrafast proton transport in sub-1-nm diameter carbon nanotube porins. *Nat. Nanotechnol.* **11**, 639–644 (2016).
22. M. Tagliazucchi, I. Szleifer, Transport mechanisms in nanopores and nanochannels: Can we mimic nature? *Mater. Today* **18**, 131–142 (2015).
23. S. Faucher, N. Aluru, M. Z. Bazant, D. Blankschtein, A. H. Brozena, J. Cumings, J. Pedro de Souza, M. Elimelech, R. Epsztein, J. T. Fourkas, A. G. Rajan, H. J. Kulik, A. Levy, A. Majumdar, C. Martin, M. McEldrew, R. P. Misra, A. Noy, T. A. Pham, M. Reed, E. Schwegler, Z. Siwy, Y. Wang, M. Strano, Critical knowledge gaps in mass transport through single-digit nanopores: A review and perspective. *J. Phys. Chem. C* **123**, 21309–21326 (2019).
24. X. Zhu, J. Hao, B. Bao, Y. Zhou, H. Zhang, J. Pang, Z. Jiang, L. Jiang, Unique ion rectification in hypersaline environment: A high-performance and sustainable power generator system. *Sci. Adv.* **4**, eaau1665 (2018).
25. Z. Zhang, L. Wen, L. Jiang, Bioinspired smart asymmetric nanochannel membranes. *Chem. Soc. Rev.* **47**, 322–356 (2018).
26. A. Siria, M.-L. Bocquet, L. Bocquet, New avenues for the large-scale harvesting of blue energy. *Nat. Rev. Chem.* **1**, 0091 (2017).
27. M. Macha, S. Marion, V. V. Nandigana, A. Radenovic, 2D materials as an emerging platform for nanopore-based power generation. *Nat. Rev. Mater.* **4**, 588–605 (2019).
28. H. Zhang, Y. Tian, L. Jiang, Fundamental studies and practical applications of bio-inspired smart solid-state nanopores and nanochannels. *Nano today* **11**, 61–81 (2016).
29. Z. Y. Jiang, H. L. Liu, S. A. Ahmed, S. Hanif, S. B. Ren, J. J. Xu, H. Y. Chen, X. H. Xia, K. Wang, Insight into ion transfer through the sub-nanometer channels in zeolitic imidazolate frameworks. *Angew. Chem.* **129**, 4845–4849 (2017).
30. J. Lu, H. Zhang, J. Hou, X. Li, X. Hu, Y. Hu, C. D. Easton, Q. Li, C. Sun, A. W. Thornton, M. R. Hill, X. Zhang, G. Jiang, J. Z. Liu, A. J. Hill, B. D. Freeman, L. Jiang, H. Wang, Efficient metal ion sieving in rectifying subnanochannels enabled by metal–organic frameworks. *Nat. Mater.* **19**, 767–774 (2020).
31. C. Wang, F.-F. Liu, Z. Tan, Y.-M. Chen, W.-C. Hu, X.-H. Xia, Fabrication of bio-inspired 2D MOFs/PAA hybrid membrane for asymmetric ion transport. *Adv. Funct. Mater.* **30**, 1908804 (2020).
32. X. Li, H. Zhang, H. Yu, J. Xia, Y. B. Zhu, H. A. Wu, J. Hou, J. Lu, R. Ou, C. D. Easton, C. Selomulya, R. M. Hill, L. Jiang, H. Wang, Unidirectional and selective proton transport in artificial heterostructured nanochannels with nano-to-subnano confined water clusters. *Adv. Mater.* **32**, 2001777 (2020).
33. A. Legrand, S. Furukawa, A selective ionic rectifier. *Nat. Mater.* **19**, 701–702 (2020).
34. M. Sánchez-Sánchez, N. Getachew, K. Díaz, M. Díaz-García, Y. Chebude, I. Díaz, Synthesis of metal–organic frameworks in water at room temperature: Salts as linker sources. *Green Chem.* **17**, 1500–1509 (2015).
35. Y. Zhou, B. Yan, Imparting tunable and white-light luminescence to a nanosized metal–organic framework by controlled encapsulation of lanthanide cations. *Inorg. Chem.* **53**, 3456–3463 (2014).
36. N. Reimer, B. Gil, B. Marszalek, N. Stock, Thermal post-synthetic modification of Al-MIL-53–COOH: Systematic investigation of the decarboxylation and condensation reaction. *CrystEngComm* **14**, 4119–4125 (2012).
37. T. Devic, P. Horcajada, C. Serre, F. Salles, G. Maurin, B. Moulin, D. Heurtaux, G. Clet, A. Vimont, J.-M. Greneche, B. L. Ouay, F. Moreau, E. Magnier, Y. Filinchuk, J. Marrot, J.-C. Lavalley, M. Daturi, G. Ferey, Functionalization in flexible porous solids: Effects on the pore opening and the host–guest interactions. *J. Am. Chem. Soc.* **132**, 1127–1136 (2010).
38. A. S. Munn, R. S. Pillai, S. Biswas, N. Stock, G. Maurin, R. I. Walton, The flexibility of modified-linker MIL-53 materials. *Dalton Trans.* **45**, 4162–4168 (2016).
39. M. R. Whorton, R. MacKinnon, Crystal structure of the mammalian GIRK2 $K^+$ channel and gating regulation by G proteins, PIP2, and sodium. *Cell* **147**, 199–208 (2011).
40. L. H. Pinto, R. A. Lamb, The M2 proton channels of influenza A and B viruses. *J. Biol. Chem.* **281**, 8997–9000 (2006).
41. M. Sasaki, M. Takagi, Y. Okamura, A voltage sensor-domain protein is a voltage-gated proton channel. *Science* **312**, 589–592 (2006).
42. A. R. Taylor, C. Brownlee, G. L. Wheeler, Proton channels in algae: Reasons to be excited. *Trends Plant Sci.* **17**, 675–684 (2012).
43. H. Zhang, J. Hou, Y. Hu, P. Wang, R. Ou, L. Jiang, J. Z. Liu, B. D. Freeman, A. J. Hill, H. Wang, Ultrafast selective transport of alkali metal ions in metal organic frameworks with subnanometer pores. *Sci. Adv.* **4**, eaaq0066 (2018).
44. J. Lu, H. Zhang, X. Hu, B. Qian, J. Hou, L. Han, Y. Zhu, C. Sun, L. Jiang, H. Wang, Ultraselective monovalent metal ion conduction in a three-dimensional sub-1 nm nanofluidic device constructed by metal–organic frameworks. *ACS Nano* **15**, 1240–1249 (2021).
45. W. M. Haynes, *CRC Handbook of Chemistry and Physics* (CRC press, 2014).
46. V. B. Myers, D. Haydon, Ion transfer across lipid membranes in the presence of gramicidin A: II. The ion selectivity. *Biochim. Biophys. Acta Biomembr.* **274**, 313–322 (1972).
47. X. Zhou, Z. Wang, R. Epsztein, C. Zhan, W. Li, J. D. Fortner, T. A. Pham, J.-H. Kim, M. Elimelech, Intrapore energy barriers govern ion transport and selectivity of desalination membranes. *Sci. Adv.* **6**, eabd9045 (2020).
48. Z. Zhang, L. Wen, L. Jiang, Nanofluidics for osmotic energy conversion. *Nat. Rev. Mater.* **6**, 622–639 (2021).
49. Y. Zhou, L. Jiang, Bioinspired nanoporous membrane for salinity gradient energy harvesting. *Joule* **4**, 2244–2248 (2020).
50. L. Wang, Z. Wang, S. K. Patel, S. Lin, M. Elimelech, Nanopore-based power generation from salinity gradient: Why it is not viable. *ACS Nano* **15**, 4093–4107 (2021).
51. X. Lin, E. Shamsaei, B. Kong, J. Z. Liu, T. Xu, H. Wang, Fabrication of asymmetrical diffusion dialysis membranes for rapid acid recovery with high purity. *J. Mater. Chem. A* **3**, 24000–24007 (2015).
52. M. German, A. K. SenGupta, J. Greenleaf, Hydrogen ion ($H^+$) in waste acid as a driver for environmentally sustainable processes: Opportunities and challenges. *Environ. Sci. Technol.* **47**, 2145–2150 (2013).
53. W. Xin, Z. Zhang, X. Huang, Y. Hu, T. Zhou, C. Zhu, X.-Y. Kong, L. Jiang, L. Wen, High-performance silk-based hybrid membranes employed for osmotic energy conversion. *Nat. Commun.* **10**, 3876 (2019).
54. Q. Zhang, P. S. Cao, Y. Cheng, S. S. Yang, Y. D. Yin, T. Y. Lv, Z. Y. Gu, Nonlinear ion transport through ultrathin metal–organic framework nanosheet. *Adv. Funct. Mater.* **30**, 2004854 (2020).
55. S. L. Mayo, B. D. Olafson, W. A. Goddard, DREIDING: A generic force field for molecular simulations. *J. Phys. Chem.* **94**, 8897–8909 (1990).
56. A. C. Van Duin, S. Dasgupta, F. Lorant, W. A. Goddard, ReaxFF: A reactive force field for hydrocarbons. *J. Chem. Phys. A* **105**, 9396–9409 (2001).
57. S. Plimpton, Fast parallel algorithms for short-range molecular dynamics. *J. Comput. Phys.* **117**, 1–19 (1995).
58. G. Henkelman, B. P. Uberuaga, H. Jónsson, A climbing image nudged elastic band method for finding saddle points and minimum energy paths. *J. Chem. Phys.* **113**, 9901–9904 (2000).

59. P. Giannozzi, S. Baroni, N. Bonini, M. Calandra, R. Car, C. Cavazzoni, D. Ceresoli, G. L. Chiarotti, M. Cococcioni, I. Dabo, A. D. Corso, S. de Gironcoli, S. Fabris, G. Fratesi, R. Gebauer, U. Gerstmann, C. Gougoussis, A. Kokalj, M. Lazzeri, L. Martin-Samos, N. Marzari, F. Mauri, R. Mazzarello, S. Paolini, A. Pasquarello, L. Paulatto, C. Sbraccia, S. Scandolo, G. Sclauzero, A. P. Seitsonen, A. Smogunov, P. Umari, R. M. Wentzcovitch, QUANTUM ESPRESSO: A modular and open-source software project for quantum simulations of materials. *J. Phys. Condens. Matter* **21**, 395502 (2009).
60. J. P. Perdew, K. Burke, M. Ernzerhof, Generalized gradient approximation made simple. *Phys. Rev. Lett.* **77**, 3865–3868 (1996).
61. H. Reinsch, N. Stock, High-throughput studies of highly porous Al-based MOFs. *Microporous Mesoporous Mater.* **171**, 156–165 (2013).
62. R. H. Tunuguntla, R. Y. Henley, Y.-C. Yao, T. A. Pham, M. Wanunu, A. Noy, Enhanced water permeability and tunable ion selectivity in subnanometer carbon nanotube porins. *Science* **357**, 792–796 (2017).
63. D.-K. Kim, C. Duan, Y.-F. Chen, A. Majumdar, Power generation from concentration gradient by reverse electrodialysis in ion-selective nanochannels. *Microfluid. Nanofluidics* **9**, 1215–1224 (2010).
64. C.-Y. Lin, C. Combs, Y.-S. Su, L.-H. Yeh, Z. S. Siwy, Rectification of concentration polarization in mesopores leads to high conductance ionic diodes and high performance osmotic power. *J. Am. Chem. Soc.* **141**, 3691–3698 (2019).
65. J. Wang, M. Zhang, J. Zhai, L. Jiang, Theoretical simulation of the ion current rectification (ICR) in nano-pores based on the Poisson–Nernst–Planck (PNP) model. *Phys. Chem. Chem. Phys.* **16**, 23–32 (2014).
66. M. Valiskó, B. Matejczyk, Z. Ható, T. Kristóf, E. Mádai, D. Fertig, D. Gillespie, D. Boda, Multiscale analysis of the effect of surface charge pattern on a nanopore's rectification and selectivity properties: From all-atom model to Poisson-Nernst-Planck. *J. Chem. Phys.* **150**, 144703 (2019).
67. L. Chen, B. Tu, X. Lu, F. Li, L. Jiang, M. Antonietti, K. Xiao, Unidirectional ion transport in nanoporous carbon membranes with a hierarchical pore architecture. *Nat. Commun.* **12**, 4650 (2021).
68. M. Meilikhov, K. Yusenko, R. A. Fischer, The adsorbate structure of ferrocene inside [Al(OH)(bdc)]x (MIL-53): A powder X-ray diffraction study. *Dalton Trans.* 600–602 (2009).
69. M. Chen, L. Zheng, B. Santra, H.-Y. Ko, R. A. DiStasio Jr., M. L. Klein, R. Car, X. Wu, Hydroxide diffuses slower than hydronium in water because its solvated structure inhibits correlated proton transfer. *Nat. Chem.* **10**, 413–419 (2018).
70. C. Volkringer, T. Loiseau, N. Guillou, G. Ferey, M. Haouas, F. Taulelle, E. Elkaim, N. Stock, High-throughput aided synthesis of the porous metal-organic framework-type aluminum pyromellitate, MIL-121, with extra carboxylic acid functionalization. *Inorg. Chem.* **49**, 9852–9862 (2010).
71. S. Chen, S. Mukherjee, B. E. G. Lucier, Y. Guo, Y. T. A. Wong, V. V. Terskikh, M. J. Zaworotko, Y. Huang, Cleaving carboxyls: Understanding thermally triggered hierarchical pores in the metal–organic framework MIL-121. *J. Am. Chem. Soc.* **141**, 14257–14271 (2019).
72. H. J. Berendsen, J. Postma, W. F. van Gunsteren, A. DiNola, J. Haak, Molecular dynamics with coupling to an external bath. *J. Chem. Phys.* **81**, 3684–3690 (1984).
73. T. Splith, E. Pantatosaki, P. D. Kolokathis, D. Fröhlich, K. Zhang, G. Füldner, C. Chmelik, J. Jiang, S. K. Henninger, F. Stallmach, G. K. Papadopoulos, Molecular dynamics phenomena of water in the metalorganic framework MIL-100 (Al), as revealed by pulsed field gradient NMR and atomistic simulation. *J. Phys. Chem. C* **121**, 18065–18074 (2017).
74. M. C. Pitman, A. C. van Duin, Dynamics of confined reactive water in smectite clay–zeolite composites. *J. Am. Chem. Soc.* **134**, 3042–3053 (2012).
75. A. K. Rappe, W. A. Goddard III, Charge equilibration for molecular dynamics simulations. *J. Phys. Chem.* **95**, 3358–3363 (1991).
76. G. Prandini, A. Marrazzo, I. E. Castelli, N. Mounet, N. Marzari, Precision and efficiency in solid-state pseudopotential calculations. *Npj Comput. Mater.* **4**, 72 (2018).
77. S. Grimme, J. Antony, S. Ehrlich, H. Krieg, A consistent and accurate ab initio parametrization of density functional dispersion correction (DFT-D) for the 94 elements H-Pu. *J. Chem. Phys.* **132**, 154104 (2010).
78. M. Yu, D. R. Trinkle, Accurate and efficient algorithm for Bader charge integration. *J. Chem. Phys.* **134**, 064111 (2011).
79. H. Yu, H. Xu, J. Fan, Y.-B. Zhu, F. Wang, H. Wu, Transport of shale gas in microporous/nanoporous media: Molecular to pore-scale simulations. *Energy Fuels* **35**, 911–943 (2021).
80. A. Beskok, G. E. Karniadakis, Report: A model for flows in channels, pipes, and ducts at micro and nano scales. *Microscale Thermophys. Eng.* **3**, 43–77 (1999).
81. F. Ragon, B. Campo, Q. Yang, C. Martineau, A. D. Wiersum, A. Lago, V. Guillerm, C. Hemsley, J. F. Eubank, M. Vishnuvarthan, F. Taulelle, P. Horcajada, A. Vimont, P. L. Llewellyn, M. Daturi, S. Devautour-Vinot, G. Maurin, C. Serre, T. Devic, G. Clet, Acid-functionalized UiO-66(Zr) MOFs and their evolution after intra-framework cross-linking: Structural features and sorption properties. *J. Mater. Chem. A* **3**, 3294–3309 (2015).
82. M. Iwamoto, H. Shimizu, I. Muramatsu, S. Oiki, A cytotoxic peptide from a marine sponge exhibits ion channel activity through vectorial-insertion into the membrane. *FEBS Lett.* **584**, 3995–3999 (2010).
83. Y. Matsuki, M. Iwamoto, K. Mita, K. Shigemi, S. Matsunaga, S. Oiki, Rectified proton Grotthuss conduction across a long water-wire in the test nanotube of the polytheonamide B channel. *J. Am. Chem. Soc.* **138**, 4168–4177 (2016).
84. X. Li, H. Zhang, J. Hou, R. Ou, Y. Zhu, C. Zhao, T. Qian, C. D. Easton, C. Selomulya, M. R. Hill, H. Wang, Sulfonated sub-1-nm metal–organic framework channels with ultrahigh proton selectivity. *J. Am. Chem. Soc.* **142**, 9827–9833 (2020).
85. H. Q. Liang, Y. Guo, Y. Shi, X. Peng, B. Liang, B. Chen, A light-responsive metal-organic framework hybrid membrane with high on/off photoswitchable proton conductivity. *Angew. Chem. Int. Ed.* **59**, 7732–7737 (2020).
86. H.-Q. Liang, Y. Guo, X. Peng, B. Chen, Light-gated cation-selective transport in metal–organic framework membranes. *J. Mater. Chem. A* **8**, 11399–11405 (2020).
87. E. Griffin, L. Mogg, G.-P. Hao, G. Kalon, C. Bacaksiz, G. Lopez-Polin, T. Zhou, V. Guarochico, J. Cai, C. Neumann, A. Winter, M. Mohn, J. H. Lee, J. Lin, U. Kaiser, I. V. Grigorieva, K. Suenaga, B. Özyilmaz, H.-M. Cheng, W. Ren, A. Turchanin, F. M. Peeters, A. K. Geim, M. Lozada-Hidalgo, Proton and Li-ion permeation through graphene with eight-atom-ring defects. *ACS Nano* **14**, 7280–7286 (2020).
88. J. Wang, Z. Zhang, J. Zhu, M. Tian, S. Zheng, F. Wang, X. Wang, L. Wang, Ion sieving by a two-dimensional $Ti_3C_2T_x$ alginate lamellar membrane with stable interlayer spacing. *Nat. Commun.* **11**, 3540 (2020).
89. L. Cao, W. Guo, W. Ma, L. Wang, F. Xia, S. Wang, Y. Wang, L. Jiang, D. Zhu, Towards understanding the nanofluidic reverse electrodialysis system: Well matched charge selectivity and ionic composition. *Energ. Environ. Sci.* **4**, 2259–2266 (2011).
90. A. Siria, P. Poncharal, A.-L. Biance, R. Fulcrand, X. Blase, S. T. Purcell, L. Bocquet, Giant osmotic energy conversion measured in a single transmembrane boron nitride nanotube. *Nature* **494**, 455–458 (2013).
91. M. I. Walker, K. Ubych, V. Saraswat, E. A. Chalklen, P. Braeuninger-Weimer, S. Caneva, R. S. Weatherup, S. Hofmann, U. F. Keyser, Extrinsic cation selectivity of 2D membranes. *ACS Nano* **11**, 1340–1346 (2017).
92. J. Feng, M. Graf, K. Liu, D. Ovchinnikov, D. Dumcenco, M. Heiranian, V. Nandigana, N. R. Aluru, A. Kis, A. Radenovic, Single-layer $MoS_2$ nanopores as nanopower generators. *Nature* **536**, 197–200 (2016).
93. G. Laucirica, M. E. Toimil-Molares, C. Trautmann, W. Marmisollé, O. Azzaroni, Polyaniline for improved blue energy harvesting: Highly rectifying nanofluidic diodes operating in hypersaline conditions via one-step functionalization. *ACS Appl. Mater. Interfaces* **12**, 28148–28157 (2020).
94. Y.-C. Liu, L.-H. Yeh, M.-J. Zheng, K. C.-W. Wu, Highly selective and high-performance osmotic power generators in subnanochannel membranes enabled by metal-organic frameworks. *Sci. Adv.* **7**, eabe9924 (2021).


**Acknowledgments:** We acknowledge the use of instruments and scientific and technical assistance at the Monash Centre for Electron Microscopy, a Node of Microscopy Australia. We thank E. Wang and Y. Liang for assistance with sample characterization. The used PET films are part of a UMAT experiment, which was performed at the beam line X0 at the GSI Helmhotzzentrum fuer Schwerionenforschung, Darmstadt (Germany), in the frame of FAIR Phase-0. **Funding:** We thank the financial support from Australian Research Council (DP170102964 and FL200100049). H.W. is the recipient of an Australian Research Council Australian Laureate Fellowship (FL200100049) funded by the Australian government. **Author contributions:** J.L. and H.W. conceived this project. J.L. designed the experiments. J.L. and X.H. fabricated samples and performed measurements and characterizations. H.X., H.Y., and J.X. did the simulations under the supervision of F.W. and H.-A.W. Y.Z. helped the characterizations. J.L. analyzed the data and wrote the manuscript. J.L., H.W., F.W., H.-A.W., H.X., X.H., and H.Y. revised the manuscript with the comments from L.J. All authors contributed to the discussions. **Competing interests:** The authors declare that they have no competing interests. **Data and materials availability:** All data needed to evaluate the conclusions in the paper are presented in the paper and/or the Supplementary Materials.

Submitted 18 July 2021
Accepted 16 February 2022
Published 6 April 2022
10.1126/sciadv.abl5070